Phoebe: A Surface Dominated by Water

Fraser, W. C., & Brown, M. E. (2018). Phoebe: A Surface Dominated by Water. *Astronomical Journal*, *156*(1), 23. https://doi.org/10.3847/1538-3881/aac213

Published in:
Astronomical Journal

Document Version:
Publisher's PDF, also known as Version of record

Queen's University Belfast - Research Portal:
Link to publication record in Queen's University Belfast Research Portal

The Astronomical Journal, 156:23 (13pp), 2018 July https://doi.org/10.3847/1538-3881/aac213

Phoebe: A Surface Dominated by Water

Wesley C. Fraser[1] and Michael E. Brown[2]
[1] Queen's University, Belfast Belfast Co. Antrim BT7 1NN, UK; wes.fraser@qub.ac.uk
[2] California Institute of Technology, USA
Received 2018 March 12; revised 2018 April 29; accepted 2018 April 30; published 2018 June 22

Abstract

The Saturnian irregular satellite, Phoebe, can be broadly described as a water-rich rock. This object, which presumably originated from the same primordial population shared by the dynamically excited Kuiper Belt Objects (KBOs), has received high-resolution spectral imaging during the *Cassini* flyby. We present a new analysis of the Visual Infrared Mapping Spectrometer observations of Phoebe, which critically, includes a geometry correction routine that enables pixel-by-pixel mapping of visible and infrared spectral cubes directly onto the Phoebe shape model, even when an image exhibits significant trailing errors. The result of our re-analysis is a successful match of 46 images, producing spectral maps covering the majority of Phoebe's surface, roughly a third of which is imaged by high-resolution observations (<22 km per pixel resolution). There is no spot on Phoebe's surface that is absent of water absorption. The regions richest in water are clearly associated with the Jason and south pole impact basins. Phoebe exhibits only three spectral types, and a water–ice concentration that correlates with physical depth and visible albedo. The water-rich and water-poor regions exhibit significantly different crater size frequency distributions and different large crater morphologies. We propose that Phoebe once had a water-poor surface whose water–ice concentration was enhanced by basin-forming impacts that exposed richer subsurface layers. The range of Phoebe's water–ice absorption spans the same range exhibited by dynamically excited KBOs. The common water–ice absorption depths and primordial origins, and the association of Phoebe's water-rich regions with its impact basins, suggests the plausible idea that KBOs also originated with water-poor surfaces that were enhanced through stochastic collisional modification.

Key words: methods: data analysis – planets and satellites: individual (Phoebe) – planets and satellites: surfaces

1. Introduction

It is generally accepted that the Saturnian irregular satellite, Phoebe, is a captured body from the outer solar system. This idea is supported by its low, ∼8% albedo, and retrograde orbit (Johnson & Lunine 2005). Orbits such as Phoebe's are a natural bi-product of capture during the early reorganization of the gas-giants, which was also responsible for the dispersal of the proto-planetesimal disk (Nesvorný et al. 2007), implying that Phoebe broadly shares the same primordial planetesimal population as the dynamically excited Kuiper Belt Objects (KBOs; Levison et al. 2008). Admittedly, Phoebe's density of $1.6\,\mathrm{g\,cm^{-3}}$ is roughly a factor of two higher than the typical densities of similarly sized KBOs (see for example Grundy et al. 2015).

During its entry into the Saturnian system, the *Cassini* spacecraft flew past Phoebe, acquiring resolved optical imaging and optical-NIR spectral imaging with the Imaging Sub System (ISS; Porco et al. 2004) and Visible-Infrared Mapping Spectrometer (VIMS). ISS imagery revealed a roughly spherical body, with a collisionally evolved surface possessing numerous large impact basins (Porco et al. 2005). The irregular satellite environments around the gas-giants are the most collisionally extreme environments in the known solar system (Bottke et al. 2010). As a result, it may be that Phoebe has undergone significantly higher bombardment than typically experienced by KBOs. This bombardment may explain Phoebe's comparatively high density.

Rough compositional mapping has been done with the VIMS observations (Clark et al. 2005; Hansen et al. 2012). Notable discoveries include the discovery of Fe-rich silicates, CO_2 ice, and water absorption (Clark et al. 2005; Coradini et al. 2008), with nonnegligible absorption of all three found across Phoebe's imaged surface (Cruikshank et al. 2010; Hansen et al. 2012). Other candidate materials include C–N organics, consistent with Phoebe's low geometric albedo. Generally, however, Phoebe's surface can be simply described as an icy rock.

KBOs exhibit a broad range of water–ice absorptions (Barkume et al. 2008; Guilbert et al. 2009; Brown et al. 2012). No hypothesis has been put forth to explain the origins of this variation. If Phoebe does indeed share a primordial origin with the excited KBOs, Phoebe's resolved spectral imaging may provide insight into the origin of this water–ice variation between KBOs.

Using an automatic technique to correct the flyby geometry of each VIMS image, we produce the first VIMS maps that are procedurally associated with Phoebe's surface. Using both the optical and IR channels of 46 VIMS images, we produce the most comprehensive compositional maps of Phoebe's surface to date. From this, we infer properties of the water distribution across Phoebe's surface. In particular, we find that Phoebe's primordial surface was likely water poor. The large basin-forming impacts that Phoebe has undergone are responsible for enhancing the surface water content through dredge-up of water-rich subsurface material. The three spectral units we have identified on Phoebe's surface exhibit water–ice absorptions compatible with the broad range of water–ice absorption exhibited by KBOs (Brown et al. 2012). This implies that large impacts may be the source of the water–ice variations seen from KBO to KBO; the KBOs that exhibit the deepest water–ice absorptions are those that have undergone the most collisional bombardment.

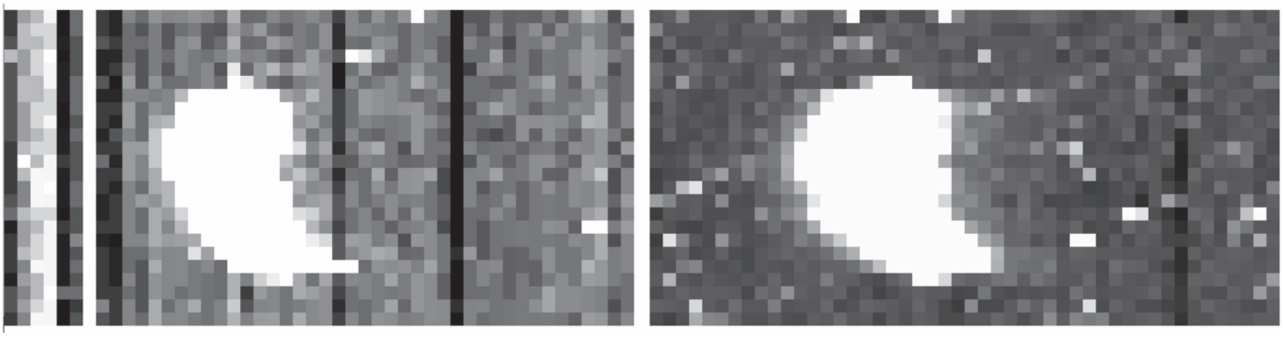

Figure 1. Visual channel 0.7 μm VIMS image before (left) and after (right) stripe removal. Scaling was set to enhance background levels.

In Section 2, we present our data analysis and mapping techniques. In Section 3, we present water absorption and crater count maps across Phoebe's surface, along with an analysis of the three spectral units we have identified. Finally, in Section 4, we discuss the origin of Phoebe's water distribution and what that implies for KBOs.

2. VIMS Data and Processing

We made use of the high- and low-resolution Visual Image Mapping Spectrometer (VIMS; Brown et al. 2004) observations of Phoebe during the approaching and receding legs of the Phoebe flyby that occurred on 2004 June 11. A number of image processing and modeling techniques were utilized to produce water absorption maps directly associated with the Phoebe shape model. A summary of these steps follows.

VIMS data were first processed through normal ISIS[3] routines to generate SPICE kernels,[4] radiometrically calibrate the raw data (RC17 calibration), and produce VIMS cubes in I/F units in the format of the Flexible Image Transport System.[5] Visual channel cubes underwent a custom stripe noise removal routine. The pixels containing only background were used to measure the median value in each image column. That value was removed from each column, and the process was then repeated for each row. This resulted in flat, de-striped, and background -removed visual channel VIMS images. An example of this de-striping is shown in Figure 1.

Manual cosmic ray and bad pixel rejection was then performed. Spectra were visibly searched for poorly behaved wavelength regions. These regions were identified by large positive and negative relative variations in the flux at that wavelength between neighboring pixels in an image. Those wavelengths were ignored.

To enable modeling of the *Cassini*–Phoebe geometry, binary images with a pixel value of 1, if that pixel contained Phoebe, and 0 if not, were produced for both channels of each VIMS image cube. Modeling of the Phoebe–*Cassini* geometry involved three iterations of a forward modeling process, in which a given Sun–Phoebe–*Cassini* geometry was used to calculate the illumination pattern directly from the medium-resolution Gaskell shape model.

Starting from the observation geometry contained in the SPICE kernel of a cube, the Sun–Phoebe–Spacecraft geometry was adjusted using a Monte Carlo Markov-chain routine to produce satisfactory matches to both the visual and IR binary images simultaneously. Free parameters in the modeling included the sub-solar longitude and latitude, the sub-*Cassini* longitude, latitude, and azimuth, and the Phoebe–*Cassini* distance at the start of an exposure. An in-image-plane linear relative velocity between Phoebe and *Cassini* was also fitted to account for tracking errors apparent in most images. All other parameters, including the Phoebe–*Cassini* velocity vector were taken as reported in the SPICE kernels. Each pixel from both channels was modeled individually to account for the small changes in the Phoebe–*Cassini*–Sun geometry that occurred while the image was gathered. For 36 images, a satisfactory geometry was found.

The satisfactorily fitted image geometries were compared to the *Cassini*–Phoebe ephemeris provided by the Jet Propulsion Laboratory (JPL) Horizons service. Systematic offsets of $1\overset{\circ}{.}5$ and $3\overset{\circ}{.}57$ in the sub-solar longitude and latitude, $7\overset{\circ}{.}71$ in the sub-*Cassini* longitude, and 6.7% in the Phoebe–*Cassini* distance were found. A second stage of geometry matching was applied to all VIMS images with the sub-solar longitude and latitude, sub-*Cassini* longitude, and Phoebe–*Cassini* distances fixed to the adjusted Horizons ephemeris. This resulted in improved matches to the binary images and enabled 10 additional images to be matched. It was found that systematic offsets of $-4\overset{\circ}{.}05$ and $8\overset{\circ}{.}75$ applied respectively to the JPL sub-*Cassini* latitude during the approaching and receding legs of the flyby provided an excellent approximation to the second stage VIMS cube matching results. A third and final match stage was run with the sub-*Cassini* and sub-solar points, and the Phoebe–*Cassini* distance fixed to the offset JPL values, resulting in slight improvements over stage two fits to most image cubes. An example of a successful fit is shown in Figure 2.

For each matched VIMS cube, individual spectra were mapped onto the facets of the medium-resolution Gaskell shape model for Phoebe. Specifically, separately for each VIMS channel, each *illuminated* facet of the medium-resolution shape model was assigned the spectrum associated with the VIMS pixel that imaged those particular facets. For each facet that was imaged three or more times, median spectra were produced for each channel. Finally, using the overlap wavelength range, the IR median spectrum of each facet was normalized to that facet's VIS median spectrum. Each facet's full-band spectrum was normalized to unity at $\lambda = 0.9$ μm and median combined to produce full VIR spectra for each imaged facet of the shape model.

A list of the 46 images for which a satisfactory geometry match could be found, along with details of each of those exposures are listed in Table 1. We group the geometry-matched

[3] https://isis.astrogeology.usgs.gov/index.html
[4] https://naif.jpl.nasa.gov/naif/data.html
[5] https://fits.gsfc.nasa.gov/fits_standard.html

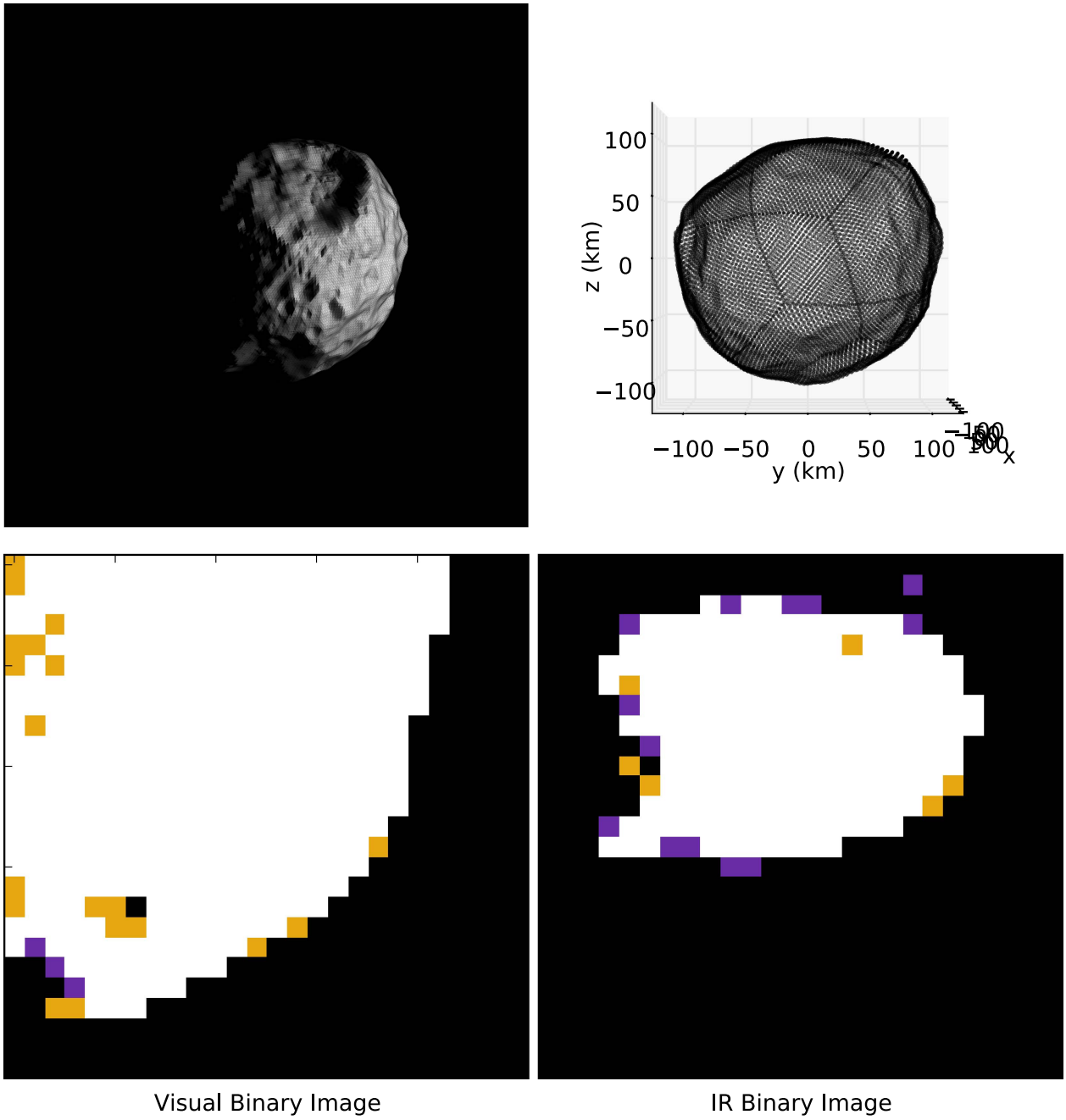

Figure 2. Shape model and binary image representations of a successful geometry modeling of cube 1465670650_1. Surface and shape model renders at the matching geometry are presented in top left and right panels. The bottom row presents the binary images (1 if a pixel contains an illuminated Phoebe, 0 otherwise) of the VIS (left) and IR (right) channels. Purple represents image pixels, orange shows model image pixels, and white shows where both model and true images contain Phoebe.

VIMS cubes into high-, medium-, and low-resolution data groups, with pixel widths at Phoebe in the IR channel of $w < 22$, $22 < w < 50$, and $w > 50$ km, respectively. When determining the spectrum of a shape model facet, the high-resolution data was utilized if that facet was sufficiently imaged by the high-resolution observations. Then, only if a facet did not yet have a median spectrum was the medium-resolution data considered, and again for the low-resolution data. In this way, the spectral resolution of the global map was as high as possible, but variable.

Relative absorption band depths were measured in the usual way, $\mathrm{BD}_\lambda = \frac{I/F_{\mathrm{cont}} - I/F_\lambda}{I/F_{\mathrm{cont}}}$ for the 1.5, and 2 μm water–ice, and 3 μm ice/hydroxyl feature. Linear continua were estimated by interpolating between the fluxes measured at 1.35, 1.78, 2.23, and 3.6 μm. The 1.5 and 2 μm features are both associated with pure water–ice, and the depths of those two features track one-to-one, as shown in Figure 3. This demonstrates that no significant variations in ice properties that could alter the relative depths of the two features, such as grain size, occur across Phoebe's surface. Thus, to increase the fidelity of the water–ice absorption map, both the 1.5 and 2 μm band depths are added together in our subsequent analysis. A small fraction of spectra with low signal-to-noise resulted in unphysical band depths. As such, any spectra with band depths that fell outside $-0.03 \leqslant \mathrm{BD}_{1.5} \leqslant 0.3$, $0.0 \leqslant \mathrm{BD}_{2.0} \leqslant 0.4$, or $0.5 \leqslant \mathrm{BD}_{3.0} \leqslant 0.85$ were rejected from further consideration.

Table 1
The Geometry of All Images for Which a Successful Geometry Could Be Determined

Image	IR Channel			Vis. Channel			C α (°)	C δ (°)	C θ (°)	S α (°)	C-P dist. (km)	V X (km)	V Y (km)	N X (km)	N Y (km)	Vel. (km s^{-1})	Vel Angle (°)
	Mode	t (s)	Res. (km)	Mode	t (s)	Res. (km)											
Low Resolution																	
1465649433_1	h	15.0	86.7	h	0.6	29.5	228.8	−19.9	5.8	321.5	173491.5	237.64	280.53	634.36	509.53	0.011	314.5
1465649746_1	h	3.8	85.9	h	0.2	29.2	226.2	−19.9	5.1	318.9	171865.4	234.83	275.08	626.96	508.32	0.069	341.6
1465649834_1	h	3.8	85.5	h	0.3	29.1	224.9	−19.9	27.3	317.6	171052.3	233.51	268.79	575.50	484.98	0.051	319.9
1465649979_1	h	3.8	85.1	h	0.2	28.9	223.6	−19.9	6.5	316.3	170239.3	251.39	282.30	574.88	499.87	0.222	304.0
1465650070_1	h	7.7	84.7	h	0.2	28.8	222.3	−19.9	4.1	315.0	169426.2	235.18	265.06	572.01	502.83	0.480	253.4
1465650234_1	h	6.0	84.1	h	0.2	28.6	220.4	−19.9	336.9	313.0	168206.6	237.82	261.99	606.75	490.15	0.103	268.1
1465650432_1	h	15.0	83.5	h	0.6	28.4	218.5	−19.9	338.7	311.1	166987.1	294.82	261.62	643.98	457.69	0.062	248.5
1465650745_1	h	3.8	82.5	h	0.2	28.0	215.2	−19.9	11.1	307.9	164954.5	209.01	252.31	542.13	449.40	0.219	326.9
1465650834_1	h	7.7	82.1	h	0.3	27.9	214.0	−19.9	9.5	306.6	164141.4	287.31	247.61	629.67	467.70	0.227	291.3
1465651001_1	h	7.7	81.7	h	0.3	27.8	212.7	−19.9	12.5	305.3	163328.4	289.89	261.22	628.01	463.72	0.305	247.6
1465651857_1	h	7.7	78.6	h	0.3	26.7	203.0	−19.9	9.0	295.6	157230.6	264.19	330.12	742.71	602.22	0.132	327.8
1465700253_2	h	15.0	85.6	h	0.6	29.1	218.6	24.8	14.6	132.8	171291.1	338.98	291.06	1133.19	328.53	0.011	5.3
1465700713_1	h	3.8	86.9	h	0.2	29.5	214.7	24.8	18.4	129.0	173730.1	345.15	309.59	1175.00	333.68	0.201	248.5
1465700837_1	h	12.0	87.5	h	0.5	29.7	212.8	24.8	16.5	127.0	174949.6	339.89	308.17	1143.69	326.59	0.371	270.6
Medium Resolution																	
1465661929_1	h	7.7	44.5	h	0.3	15.1	95.0	−19.8	348.5	186.9	88941.4	191.21	151.68	462.08	316.27	0.061	316.4
1465662167_1	h	15.0	43.7	h	0.6	14.8	92.4	−19.8	341.9	184.3	87315.8	175.49	148.95	424.73	299.01	0.135	259.0
1465662631_1	h	3.8	42.2	h	0.2	14.4	87.9	−19.8	350.7	179.8	84470.9	164.61	145.83	420.46	297.76	0.329	310.4
1465662929_1	l	19.0	40.8	h	0.6	41.6	83.5	−19.8	4.8	175.2	81626.1	396.99	580.30	309.04	288.73	0.547	275.8
1465663363_1	l	9.6	39.6	h	0.3	40.4	79.6	−19.8	8.3	171.4	79187.8	357.21	537.87	296.58	280.11	0.186	270.1
1465664556_1	l	4.8	35.7	h	0.2	36.4	67.5	−19.8	347.1	159.1	71466.8	332.83	493.61	275.93	263.48	0.302	170.4
1465664774_1	h	9.6	34.9	h	0.3	11.9	65.0	−19.8	345.8	156.5	69841.5	127.83	54.96	351.51	134.01	0.149	152.3
1465665036_1	h	15.0	34.1	h	0.6	11.6	62.4	−19.8	330.2	153.9	68216.2	139.50	56.56	336.76	135.08	0.085	218.9
1465665440_1	h	3.8	32.7	h	0.2	11.1	58.0	−19.7	341.1	149.4	65372.0	65.65	78.24	251.50	201.28	0.018	256.3
1465665563_1	h	3.8	32.3	h	0.2	11.0	56.7	−19.7	339.7	148.1	64559.4	160.35	80.58	352.10	191.66	0.042	283.4
1465665771_1	h	23.0	31.7	h	0.6	10.8	54.8	−19.7	0.7	146.1	63340.5	121.93	147.14	330.74	293.23	0.598	272.1
1465666573_1	l	12.0	28.6	h	0.3	29.2	45.3	−19.7	326.4	136.4	57246.7	393.27	474.79	330.67	265.36	0.048	252.9
1465667330_1	h	4.0	26.4	h	0.1	9.0	38.4	−19.7	318.4	129.3	52778.6	185.56	163.17	453.77	290.99	0.288	283.9
1465667721_1	h	19.0	24.8	h	0.6	8.4	33.4	−19.6	357.0	124.1	49529.5	139.26	58.58	368.49	131.84	0.028	251.5
High Resolution																	
1465669068_1	h	10.0	20.3	h	0.2	6.9	19.8	−19.6	344.9	109.9	40597.3	177.34	124.46	456.47	240.97	0.515	88.8
1465669741_1	h	4.8	18.1	h	0.2	6.1	13.1	−19.5	345.0	102.8	36133.4	24.51	12.92	147.41	69.80	0.163	301.4
1465669944_1	h	5.0	17.5	h	0.2	5.9	11.3	−19.5	335.2	100.8	34916.4	163.47	29.84	278.77	76.56	0.129	300.0
1465670212_1	l	15.0	16.2	h	0.3	16.6	7.7	−19.4	2.5	97.0	32482.9	193.01	313.06	160.58	144.58	0.452	277.7
1465670650_1	l	7.7	15.0	h	0.2	15.3	4.2	−19.4	3.5	93.1	30050.3	171.67	427.40	150.56	267.49	0.111	288.1
1465671285_1	l	1.0	13.0	l	0.1	13.3	358.4	−19.3	351.5	86.6	25998.9	186.80	42.48	170.88	37.63	0.205	158.6
1465671448_1	l	1.0	12.4	l	0.1	12.6	356.7	−19.2	6.6	84.7	24784.4	7.54	87.84	−2.01	86.74	0.565	252.4
1465671822_1	l	9.4	11.2	h	0.3	11.4	353.4	−19.2	1.8	80.8	22357.0	160.42	166.51	138.82	93.65	0.423	274.5
1465672161_1	l	9.4	10.0	h	0.3	10.2	350.3	−19.0	350.0	76.9	19932.6	103.01	100.92	85.80	27.27	0.149	88.2
1465673600_1	l	2.6	5.2	l	0.2	5.3	341.2	−17.9	325.2	61.4	10305.6	67.79	−44.15	74.66	−66.69	0.173	310.3
1465677443_1	h	10.0	8.1	h	0.2	2.7	98.0	25.6	71.2	20.0	16149.5	69.98	65.53	136.23	124.61	0.166	284.4
1465677670_1	h	10.0	8.9	h	0.2	3.0	96.2	25.5	52.9	17.4	17760.2	82.08	79.43	131.94	144.11	0.262	289.3

Table 1
(Continued)

Image	IR Channel			Vis. Channel			C α (°)	C δ (°)	C θ (°)	S α (°)	C-P dist. (km)	V X (km)	V Y (km)	N X (km)	N Y (km)	Vel. (km s^{-1})	Vel Angle (°)
	Mode	t (s)	Res. (km)	Mode	t (s)	Res. (km)											
1465678419_1	l	17.0	11.7	h	0.4	11.9	89.0	25.4	57.0	8.3	23414.2	149.44	304.52	192.06	140.61	0.309	165.2
1465678911_1	l	7.7	13.1	h	0.2	13.4	85.1	25.3	72.8	3.8	26247.3	134.89	332.74	148.61	152.18	0.245	127.5
1465679413_1	l	1.3	14.7	h	0.3	15.0	80.5	25.2	84.0	358.6	29488.1	136.31	289.02	156.90	125.14	0.028	293.0
1465679675_1	l	5.8	15.6	h	0.2	15.9	78.2	25.2	81.4	356.0	31109.4	104.41	301.79	134.42	139.35	0.215	260.1
1465679932_1	h	18.0	16.4	h	0.4	5.6	75.8	25.2	79.7	353.4	32731.2	−13.12	191.41	291.15	241.92	0.305	249.3
1465680977_2	h	18.0	21.0	h	0.4	7.2	61.8	25.1	85.3	338.6	42062.9	228.57	200.53	585.70	235.91	0.375	102.2

Note. C, S, and P refer to the *Cassini* spacecraft, the Sun, and Phoebe. X and Y are the horizontal and vertical shifts of Phoebe from the bottom left corner of the VIMS visible (V) and NIR (N) detectors, respectively. α, β, and θ correspond to longitude, latitude, and azimuth, respectively. The reported sub-*Cassini* and sub-solar α and β values, and the C-P distance are the adjusted values from the JPL Horizons ephemeris as described in Section 2. The sub-solar latitude had value, $\beta = -12\overset{\circ}{.}2$ for all observations. Modes h and l correspond to high and normal VIMS resolution modes, respectively.

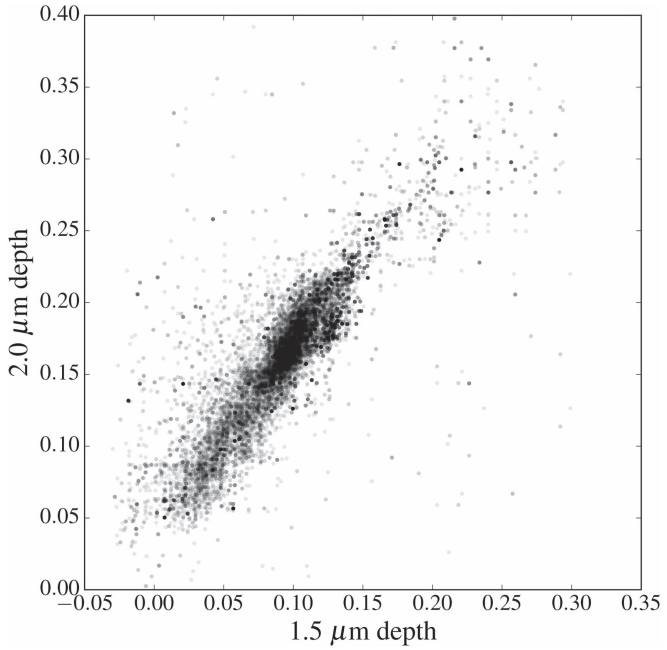

Figure 3. 1.5 and 2 μm absorption band depths of all vertices sampled in the high-resolution VIMS data group.

It should be noted that we made no attempt to correct for the effects of observing phase. A target's observed band depths seem to vary as a function of phase angle, p. The dependence on phase appears to depend on the target's albedo and composition, the wavelength of the absorption feature, and the range of phases over which the object is observed (e.g., Sanchez et al. 2012). As all VIMS data were acquired over a very small range of oblique phase angles, $84.9 < p < 91.^{\circ}3$, the relative band depth variations in the maps we present here are not affected as such. We discuss this further below.

From the band depth values, simple cylindrical projection absorption maps were produced using each facet's mean latitude and longitude with respect to the shape model center. We chose to forgo any attempts to extract specific water abundances through spectral modeling as determining correct abundances depends on knowing the exact chemical and physical properties of Phoebe's surface. Rather, we restrict our discussion purely to absorption depths.

Albedos were assigned to each facet of the shape model using the comparatively low-resolution albedo map produce from visible *Voyager* imaging of Phoebe (Simonelli et al. 1999). No higher-resolution albedo map had been produced utilizing the *Cassini* flyby data. The mean latitude and longitude of each shape model facet was calculated with respect to the shape model origin, and an albedo for that facet was sampled from that latitude and longitude on the *Voyager* albedo map.

Craters were counted in a very simple fashion, using the high-resolution surface map[6] produced by the *Cassini* Imaging Team. Craters were manually identified and their radii measured directly off the map. Only crater-like features with radii at least 3 pixels (798 m on Phoebe's surface) were counted. While the count was performed across the entire map, the smallest craters were only detectable in the highest resolution regions (longitudes, $0 \leqslant L \leqslant 90^{\circ}$). To avoid significant uncertainty in crater radius, we limited our analysis of the crater size frequency distribution to those craters with radii larger than 5 image pixels, or 1.15 km at zero degrees latitude. A more robust and complicated approach would be to count directly from the ISS images after a deprojection, rather than the global image mosaic. That more complicated approach, while not affecting the identification of large craters, would enable more reliable detection and more accurate radius measurement of the small, $r \lesssim 0.8$ km, craters. This extra level of complication would not however, afford a different interpretation to be made regarding the variation in the density of craters with radii $1 \lesssim r \lesssim 3$ km between water rich and poor regions. We opt to forgo this unnecessary level of complication.

To understand the distribution of water in Phoebe, we consider a simple global shape from which depth can be measured. Phoebe's shape is nearly ellipsoidal, with only the impact basins showing deviations away from ellipsoidal shape of more than a few kilometres. To demonstrate this, a triaxial ellipsoid was fit to the Phoebe shape model. The ellipsoid shape, rotation, and origin were allowed to vary until the root-mean-square (rms) residual value between the Gaskell shape model and the ellipsoid was at a minimum. The best-fit ellipsoid had an rms of 3.0 km, and had shape parameters, $a = 107.7$ km, $b = 107.7$ km, and $c = 104.1$ km. This fit avoided the Jason and south pole impact basins, though it should be noted that their inclusion in the fit had almost no affect at all, resulting in a nearly identical shape ($a = 107.1$ km, $b = 107.0$ km, and $c = 105.0$ km) and rotation of the ellipsoid, though with a larger rms of 4.1 km. Depth of each shape model facet was evaluated as the distance between the facet and the best-fit ellipsoid along the line that connected the ellipsoid origin and the facet itself. Virtually identical depths were found when using either fitted ellipsoid or even a sphere of radius equal to the mean radius of Phoebe (106.6 km).

For ease of presentation, we emphasize multiple distinct regions covered by the high-resolution data group: the Jason impact basin, the water-poor regions east and west of Jason which occupy a similar latitude range, and the water-rich region south of the Jason impact basin. We also point out the south pole impact basin, which is predominantly covered by the medium- and low-resolution data, a region where water absorption appears strongest.

3. Mapping Results

In the following sections, we present our cylindrical absorption band depth, albedo, and crater density maps. We discuss each of these maps in turn.

3.1. Spectra and Spectral Maps

Full water absorption depth maps are presented in Figure 4. The color scale was chosen to emphasize structure in the maps. In Figure 5, we present the water–ice absorption color map projected onto the Phoebe shape model.

Generally, we confirm the broad findings of Clark et al. (2005) in that water is found everywhere on Phoebe; there is no region with spectra completely devoid of the 1.5, 2, and 3 μm features. Our maps roughly produce a similar distribution of water across Phoebe's surface as those of Hansen et al. (2012). Though with the broader coverage of our maps, additional details can be seen. The regions richest in water are clearly associated with the impact basins, with the iciest areas found just beyond the outer edges of the Jason and south pole basins. The floor of the south pole basin exhibits significantly deeper

[6] http://www.ciclops.org/view/1743/Map-of-Phoebe–December-2005

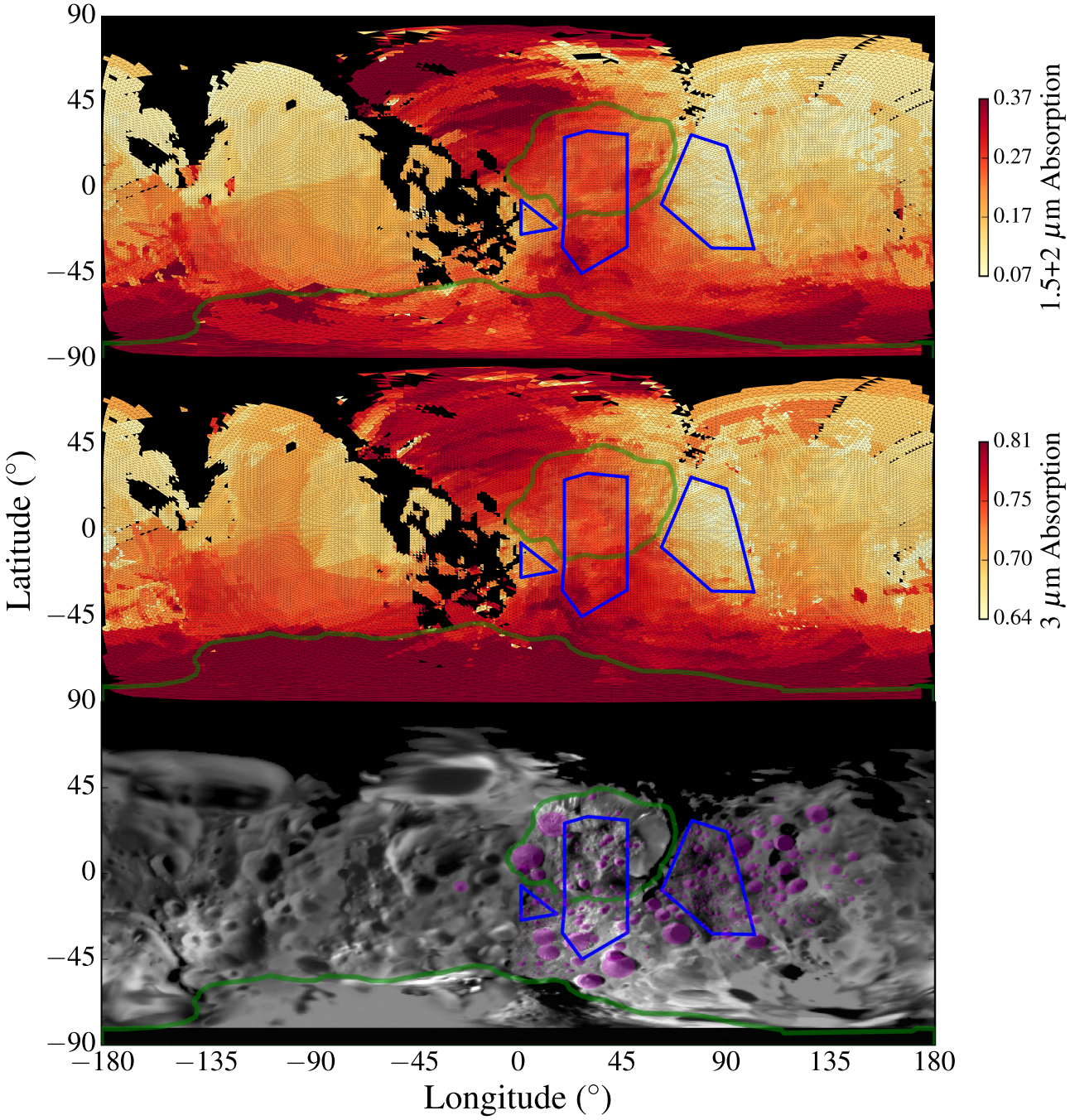

Figure 4. Water absorption band depth and optical image maps. 1.5 + 2 μm absorption band depth is shown in the top panel, and the 3 μm absorption depth is shown in the middle panel. Traced on the bottom map are the two basin edges shown in green. The locations of all craters counted in the high-resolution data are marked by the purple circles. The two water-poor (left and right) and water-rich (middle) regions from which high-resolution crater radius functions are generated are outlined in blue. Note the high latitudinal coverage of these maps are a result of illumination of Phoebe's nonspherical northern region, and not in contradiction with the sub-solar latitude of −12.°2 during the flyby.

3 μm absorption than found inside Jason Basin. The majority of water is concentrated in a ∼70° wide nearly latitudinal strip encompassing both impact basins (Figure 5).

We consider the possibility that the features apparent in the water absorption maps, and in particular, the transition from the water-rich regions near the basins, to the water-poor regions away from the basins are the result of observing geometry affecting overall band depth measurements. In Figure 6, we present four maps each made from an individual cube, covering the range of different observing geometries spanned by the VIMS data. Importantly, the top two maps are from the approaching leg, while the bottom two are from the receding leg, and hence have the relative Sun-*Cassini* orientation swapped. Despite the large variation in observing geometries displayed, the transition from water-rich to poor regions is apparent in all four maps and occurs in the same regions on Phoebe's surface. The depth, shape, and location of this feature is maintained throughout the entire VIMS data set. The same is true for the water-poor region to the west of Jason Crater. Clearly, the features in the map are real variations on Phoebe's surface and not the result of observing geometry.

We present the 1.5 + 2 μm band depth versus the 3 μm feature band depth, and albedo in Figure 7. Unlike the findings

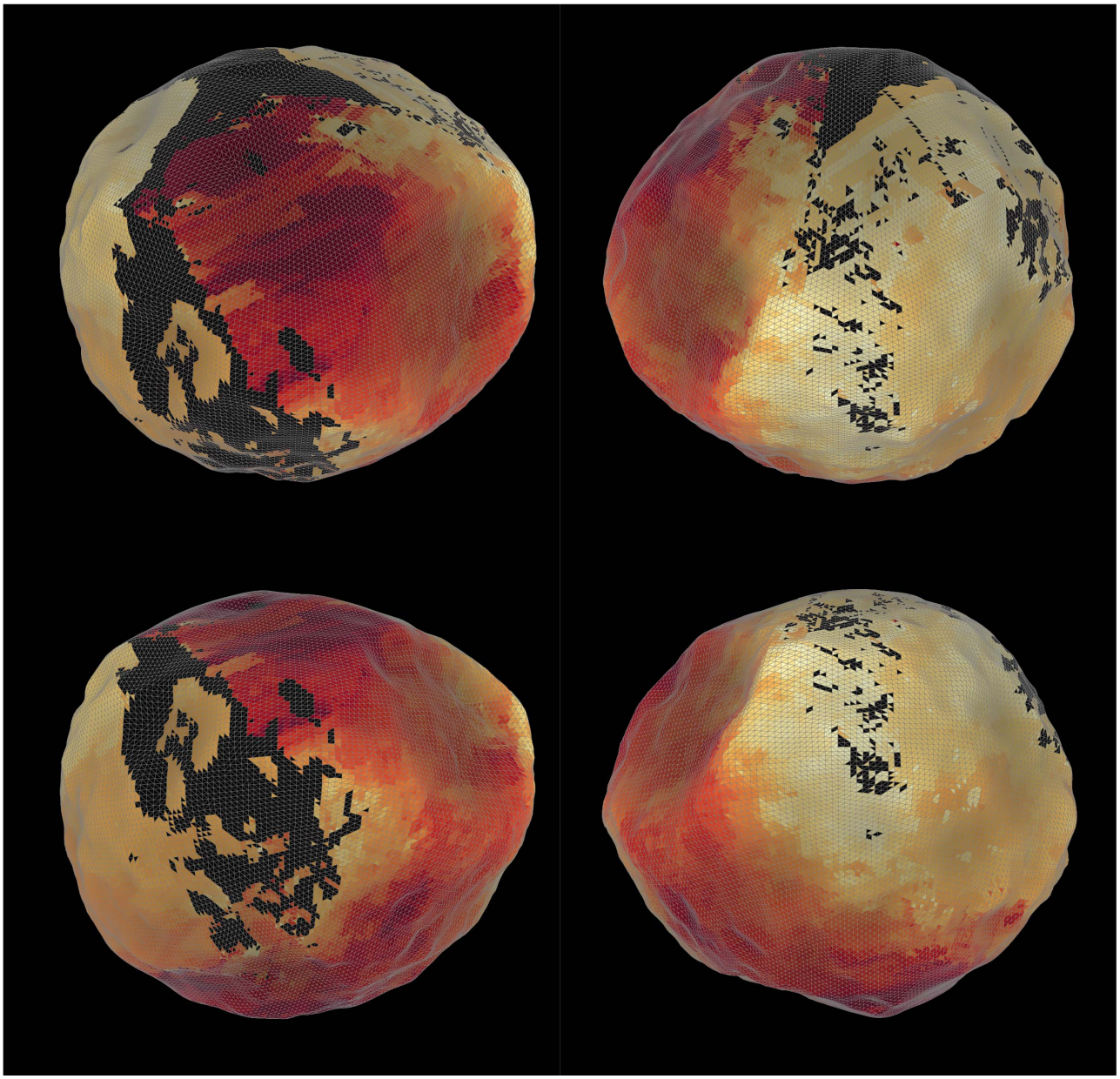

Figure 5. Water–ice absorption projected onto the medium-resolution shape model. The color scale is the same as that used in Figure 4. The sub-viewer longitudes are −15° (left) and 87° (right) and latitudes are 35° (top) and −10° (bottom) and were chosen to show all faces of Jason Crater.

of Clark et al. (2005), who found Phoebe to exhibit increasing water content with depth, we find the opposite. The majority of Phoebe's surface exhibits a clear trend of increasing water absorption with physical depth, both locally and globally. While physical depth cannot be mapped to water absorption uniquely, each distinct region generally exhibits the same positive correlation between water absorption and physical depth. The only exception is Jason crater, which exhibits water-rich walls, and a less rich crater floor (see Figure 5). This aspect of Jason crater led Clark to conclude that Phoebe's surface layers are richer in water than the subsurface layers. For any other region, and globally, the opposite is certainly true.

Phoebe's surface exhibits positively correlated water–ice and ice/hydroxyl band depths. From water content considerations, Phoebe exhibits only three spectral types. The majority of the surface falls along a tight linear continuum with water-rich and water-poor end members (see Figure 7). The average end member spectrum, including an intermediate spectrum are presented in Figure 8. As shown in that figure, the linear trend of ice and hydroxyl absorption depth, and indeed the vast majority of spectral behavior along that trend can be very simply accounted for by a geographic mixture of the two end members. Only a small fraction of Phoebe's surface is of a third type and is not a product of a mixture of the other two. Rather, these icy regions posses deeper 1.5 and 2 μm absorption depths than even the water-rich regions. These spots, predominantly found on shiny basin walls, are particularly icy compared to their surroundings. The spectra of these regions can broadly be

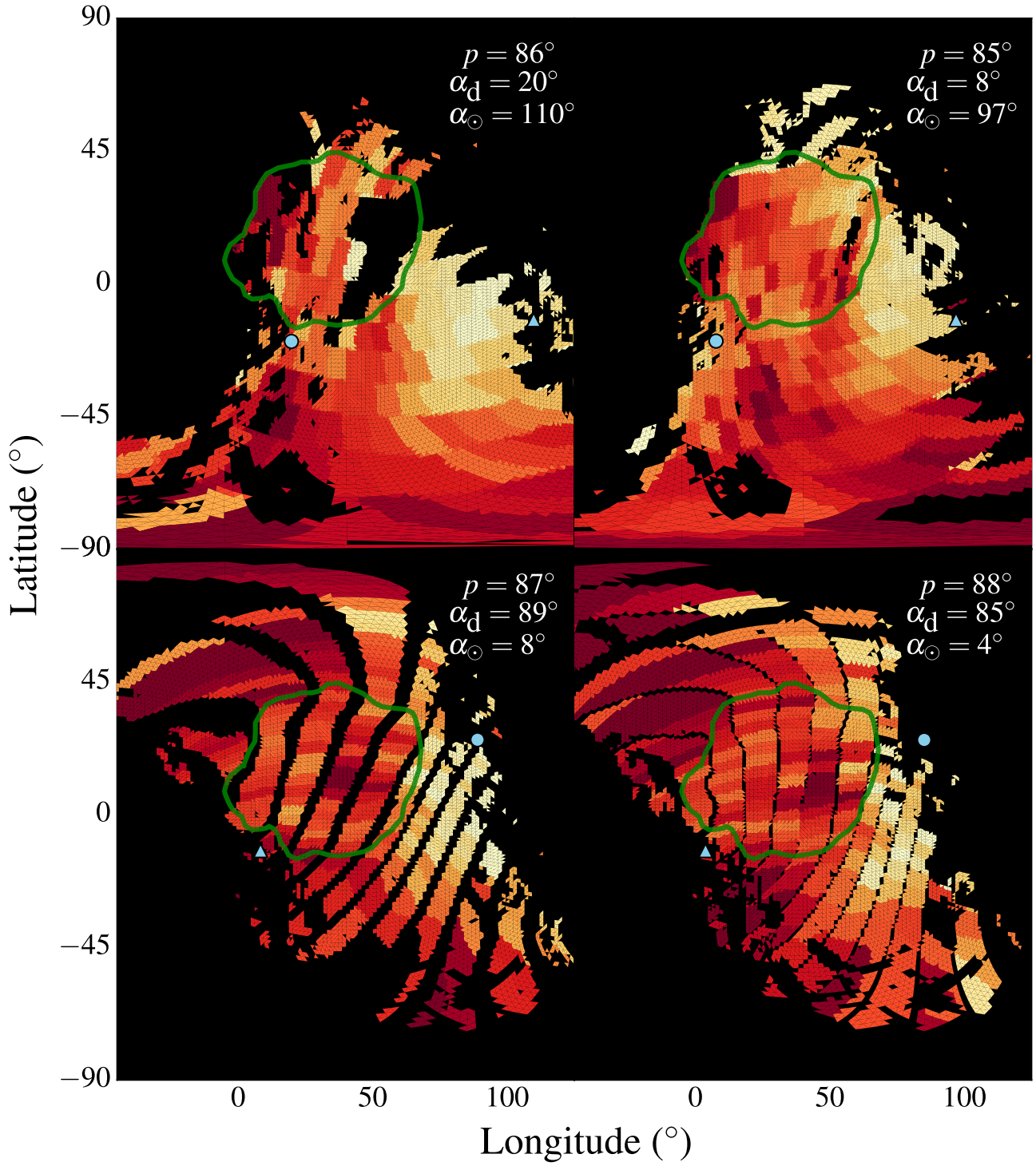

Figure 6. Water–ice absorption for individual cubes. Clockwise from top-left 1465669068_1, 1465670212_1, 1465678419_1, and 1465678911_1. The top two were acquired during the inbound leg, and the bottom two on the outbound leg. The sub-solar and sub-*Cassini* points are marked by the blue triangle and circle, respectively, with sub-longitudes and phase angle p labeled. For reference, Jason basin is traced by the green curve. Color scale is the same as that in Figure 4. The transition from water-rich (red) to water-poor (yellow) region on the east edge of Jason basin is apparent in all four maps. The orientation of the water-rich and poor regions does not depend on the relative orientation of the sub-*Cassini* and sub-solar points, demonstrating that these features are not the result of phase effects, but rather, real features on Phoebe's surface.

accounted for by a geographic mix of the rich surface end member and pure crystalline water–ice (see Figure 8).

As shown in Figure 7, visual albedo generally correlates positively with water–ice absorption depth. This implies that the presence of water, in ice form, largely governs the visual albedo. We caution against drawing further conclusions from the specific structures seen in the water–ice versus albedo plot, as the *Voyager* albedo map is of a poor resolution compared to the absorption maps. It is unclear how much of the plot's fine structure is real.

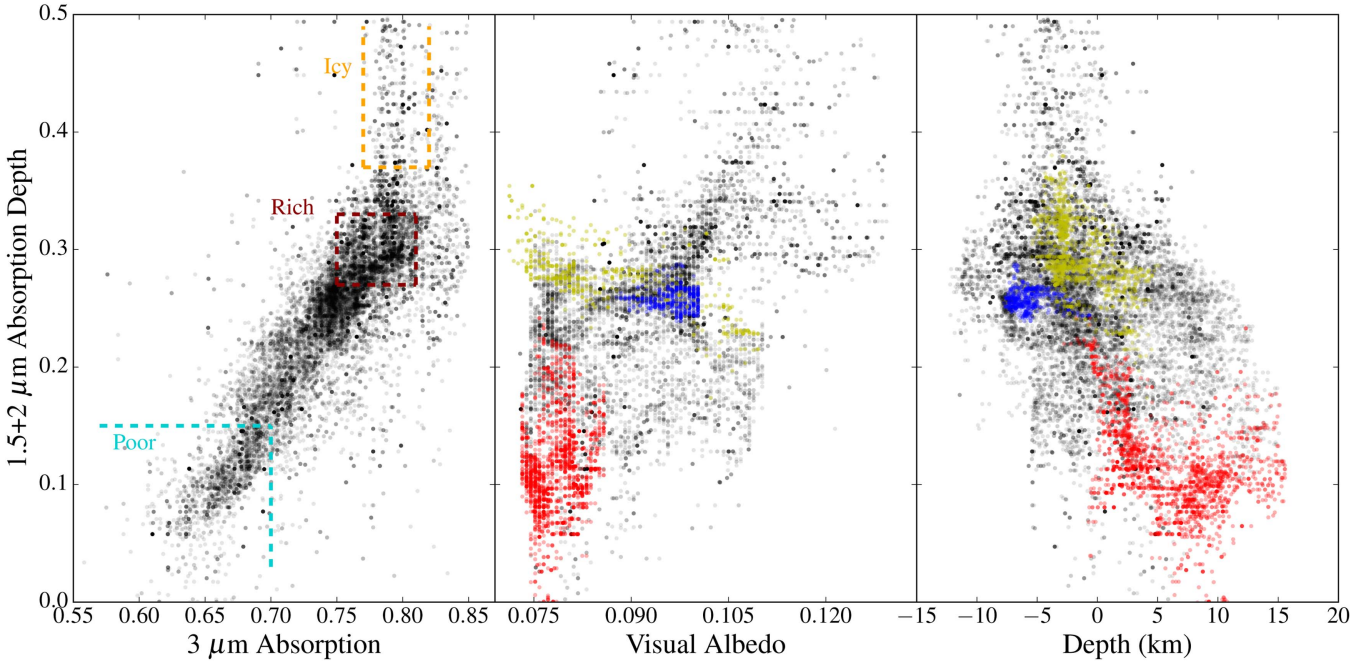

Figure 7. Band depth vs. band depth, albedo and elevation. The regions in which average spectra were generated for the poor, rich, and icy spectral types are plotted. In the middle and left plots, the blue, yellow, and red points are sampled from inside Jason Crater, the water-rich region south of Jason, and the water-poor region to the east of Jason, respectively. Only the points from facets covered by the high-resolution VIMS data group are presented.

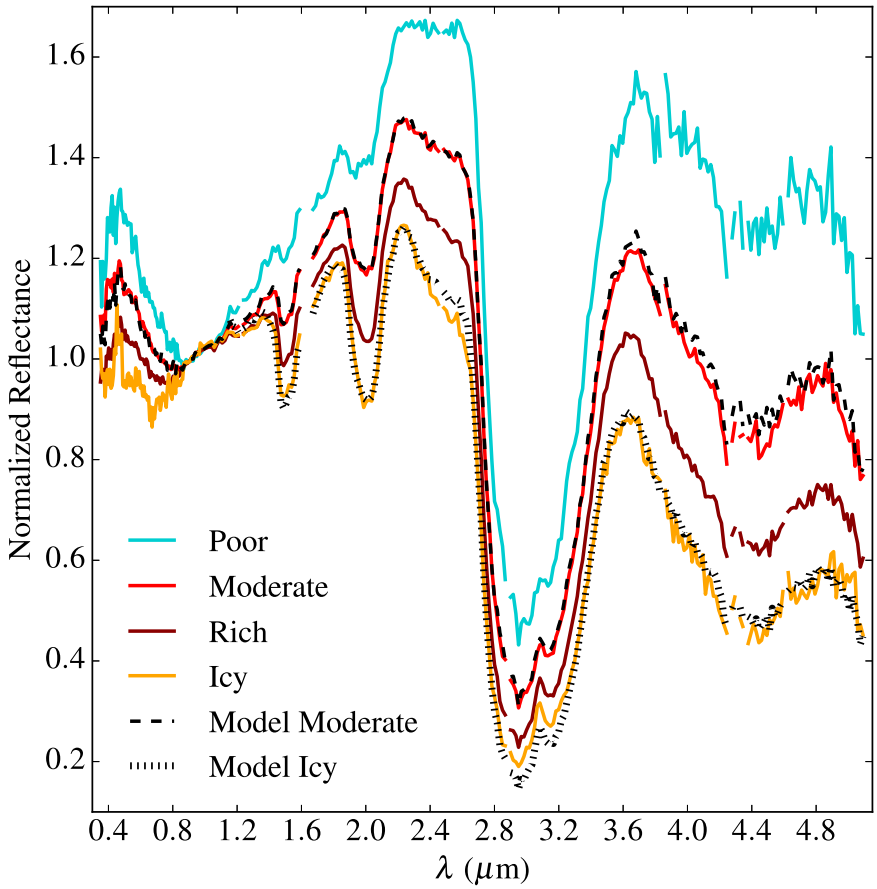

Figure 8. Spectra of the different spectral types (see Figure 7) normalized at $\lambda = 0.9$ μm. The moderate spectrum is the median of all spectra with $0.17 < BD_{1.5} < 0.25$ and $0.69 < BD_{2.0} < 0.77$. Modeled spectra of the moderate and icy spectral types are shown in the dashed and hashed lines, respectively.

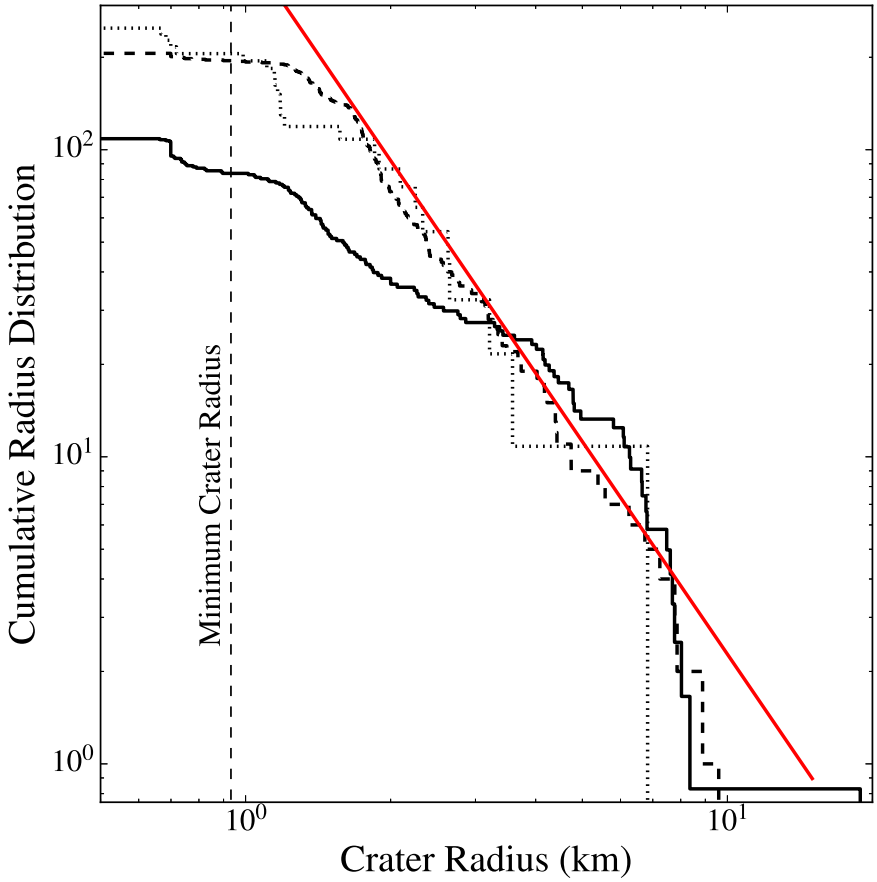

Figure 9. Cumulative crater distributions. Dashed and dotted lines demark the crater counts in the water-poor regions east and west of Jason, while the solid line demarks the counts and the water-rich regions inside and to the south of Jason. The distributions have been scaled by the ratio of their areas and the area of the larger water-poor region. The red line has slope $q = -2.3$.

3.2. Crater Counts

While we counted craters across the entire surface map, we limit our discussion to the regions with the highest ISS image resolution; Jason basin and south of Jason basin, and in the water-poor regions to the east and west. These regions and counted craters are marked in Figure 4. We present crater cumulative radius distributions (CRD) in Figure 9. The CRDs we produce are broadly compatible with past crater counting efforts (Porco et al. 2005). No significant variations in the water-rich crater CRDs inside or south of Jason basin were found. The water rich and poor regions exhibit dramatically different crater CRDs. While water-rich and poor regions exhibit a nearly equal density of craters with radii $r \gtrsim 5$ km, the water-poor regions are much richer in smaller craters possessing nearly 2.5 times more craters with $r \sim 1$ km than the water-rich regions. Furthermore, the water-poor CRD is nearly collisional, being well represented by a power-law distribution $N(>r) \propto r^{-q}$ with slope of $q \sim -2.3$. The water-rich CRD exhibits an inflection at $r \sim 5$ km from a steeper than collisional slope to a shallower than collisional distribution with slope $q \sim -1$. For craters larger than our completion limit, the Kolmogorov–Smirnoff test suggests that the probability that the area-normalized CRDs of the water-rich and poor regions are drawn from the same parent distribution is only 0.006%. It is clear even from our simple crater counting method that the water-poor regions have significantly higher small crater density than do the water-rich regions.

Beyond simple crater counts, visibly the largest craters differ in profile between the water-rich and poor regions. While slumping is apparent in the largest craters across the entirety of Phoebe, the crater size at which crater wall slumping is apparent is significantly smaller in the water-rich region. That is, moderately sized craters appear much more conical in shape than similar sized craters in the water poor region.

It is only reasonable that the impactor distribution on Phoebe is broadly homogeneous, with no preference for small objects to impact either water-rich or poor regions. It seems likely therefore, that both terrain types share roughly the same crater formation distributions. The difference in crater CRDs and the difference in shapes of larger craters appear to be the the result of water content, resulting in different rheologies for the two terrain types. It seems that water–ice acts as a lubricant, allowing slumping and small crater hiding—possibly driven through impact induced Phoebe quakes—to occur more readily.

4. Origin of Phoebe's Water Distribution

The clear concentration of water in and around Phoebe's two large impact basins argues that the impacts that formed those basins have modified the water distribution, enhancing water absorption on Phoebe's surface. The positive correlation of depth and water absorption suggests a plausible scenario that the early Phoebe possessed a water-poor surface, with richer subsurface layers. The two large basin-forming impacts then

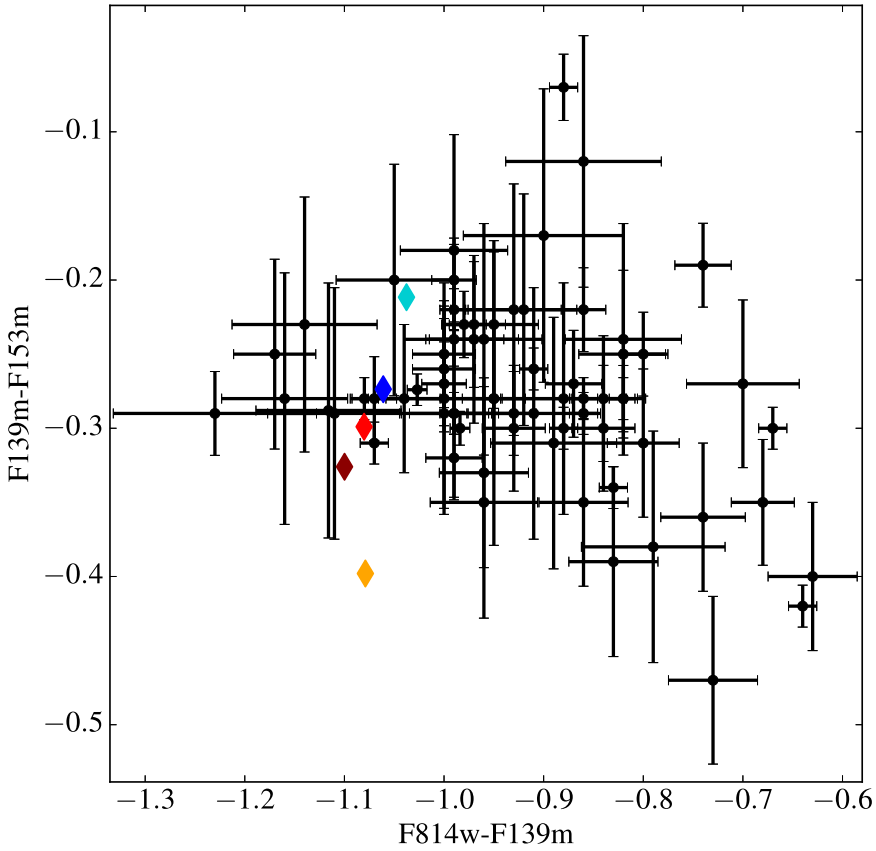

Figure 10. Observed *HST* NIR and water–ice absorption colors of small KBOs and simulated Phoebe colors (diamonds). The simulated points have been colored to match the spectra presented in Figure 8. The color of the average Phoebe spectrum is shown by the red diamond.

exposed those deeper, water-rich layers, and enhanced the water content of the regions surrounding those basins.

Surface water–ice is stable at Saturn's distance from the Sun. As has been suggested from dynamical considerations, Phoebe plausibly originated from a reservoir of planetesimals that was beyond Saturn's current orbit (Nesvorný et al. 2007) and therefore is unlikely to have spent long durations with significantly warmer surface temperatures than it has experienced since capture by Saturn. It would follow that Phoebe's originally low surface water concentration was not from post-formation heating, but rather, a property it possessed while residing in the planetesimal reservoir from which it came. It seems reasonable to expect that the majority of objects such as the Jupiter Trojans and KBOs that originated from the same population as Phoebe also originally possessed equally water-poor surfaces.

Between the epoch of formation and their scattering into the outer solar system, KBOs are unlikely to have experienced hotter temperatures than Phoebe's current surface temperature. Therefore, like Phoebe, sublimation processes are unlikely to have affected the surface water concentrations on KBOs. The broad range of water–ice absorptions exhibited by KBOs (see for example Barkume et al. 2008; Brown et al. 2012) is broadly compatible with the variation in absorptions across Phoebe's surface. To compare the range of water–ice absorptions exhibited by Phoebe's different spectral types and that of KBOs, we estimated the colors of those spectral types in the *Hubble Space Telescope* filter system using the *synphot* routine of the *stsdas IRAF* package. In Figure 10, we plot the (F814w–F139m) color versus the (F139m–F153m) color. The former of the two colors provides a measure of the NIR continuum color, while the latter is sensitive to the 1.5 μm water–ice absorption feature. Alongside the colors of Phoebe's spectral types, we plot the observed colors of a large sample of KBOs in Figure 10 (Fraser et al. 2015). Observations of asteroids at similar wavelengths to the 1.5 μm water–ice feature suggest that the band depths at $p \sim 90°$ like in the *Cassini* observations may be $\sim$5% deeper than at $p \sim 1°$ like typical for observations of KBOs (Sanchez et al. 2012). Though ground-based spectra of Phoebe acquired at $p = 6°$ present a $BD_{1.5} \simeq 10\%$ (Brown 2000), which is near the median of values measured from the *Cassini* observations (see Figure 3), suggesting that phase effects, which may alter inferred band depths do not invalidate the broad comparison between Phoebe and KBOs that we present in Figure 10.

Phoebe's surface exhibits the same range (F139m–F153m) color as do small KBOs. In particular, the color of the water-rich and water-poor spectral types match the colors of the bluest and reddest KBOs, respectively. Broadly, this implies that KBOs exhibit a range of water–ice concentrations similar to that observed on Phoebe. If Phoebe and the dynamically excited KBOs share the same primordial origins, it seems plausible that large basin-forming impacts could be responsible for enhancing the water–ice concentrations on KBOs like has occurred on Phoebe. The stochastic nature of those impacts is compatible with the observation that not all KBOs exhibit equal levels of water–ice absorption. This idea would imply that KBOs with the highest water–ice concentrations are those that experienced the highest levels of collisional dredge up. KBOs with the lowest water–ice concentrations possess old

surfaces that have undergone little to no collisional dredge up. An extreme version of this idea is perpetuated by the Haumea collisional family, the members of which are purported to be ejecta fragments of the large KBO Haumea (Brown et al. 2007). Those fragments and Haumea itself exhibit the deepest water–ice absorptions of any KBO, implying a deep dredge-up origin for those objects. Other observed KBOs have not undergone equally catastrophic collisions capable of the dramatic re-surfacing Haumea experienced.

Beyond Phoebe's gray/blue optical color, a notable difference exists between Phoebe and other small KBOs; other than the Haumea family members, small KBOs exhibit optical and NIR continuum colors that anti-correlate with the (F139m–F153m) color (Fraser & Brown 2012). Put another way, within a KBO compositional class, the redder a KBO, the more water–ice absorption it exhibits (Brown et al. 2012). Phoebe does not show this behavior, exhibiting no appreciable change in NIR continuum color, (F814w–F139m) for any of its spectral types. Moreover, Phoebe exhibits significantly bluer optical colors than do KBOs. It is hypothesized that KBOs possess organic materials that are associated with the water–ice components on those bodies (Fraser & Brown 2012). This results not only in their red colors but also the correlation between the extremity of a KBOs redness and its water–ice absorption depth. What ever organics are responsible for the red optical colors of KBOs, it is clear this material does not exist in any appreciable quantities on Phoebe's surface. The heavy collisional bombardment Phoebe has experienced in the Saturnian environment may be responsible for the removal of this material. It has been observed that some centaurs lose their red coloring and transition to purely neutral surfaces at a similar point to when they dynamically transitioned from the centaur region to the Jupiter family comet region (Jewitt 2015), a similar heliocentric distance to Saturn. It may be then that what ever thermal processes cause centaurs to lose their coloring could also have acted on Phoebe, resulting in its neutral surface color.

The authors would like to thank Pedro Lacerda for his useful insights during discussions of this work. This research has made use of the USGS Integrated Software for Imagers and Spectrometers (ISIS). STSDAS is a product of the Space Telescope Science Institute, which is operated by AURA for NASA Raw data were generated at the Planetary Data System *Cassini* Archive (http://pds-atmospheres.nmsu.edu/data_and_services/atmospheres_data/Cassini/Cassini.html). Processed data products are available from the corresponding author upon request (wes.fraser@qub.ac.uk). WCF acknowledges support from Science and Technologies Funding Council grant ST/P0003094/1. M.E.B. and W.C.F. acknowledge support from the National Aeronautics and Space Administration *Cassini* Data Analysis program grant NNX10AF11G.

Software: USGS Integrated Software for Imagers and Spectrometers, Image Reduction and Analysis Facility (Tody 1993), Space Telescope Science Data Analysis System.

ORCID iDs

Wesley C. Fraser https://orcid.org/0000-0001-6680-6558
Michael E. Brown https://orcid.org/0000-0002-8255-0545

References

Barkume, K. M., Brown, M. E., & Schaller, E. L. 2008, AJ, 135, 55
Bottke, W. F., Nesvorný, D., Vokrouhlický, D., & Morbidelli, A. 2010, AJ, 139, 994
Brown, M. E. 2000, AJ, 119, 977
Brown, M. E., Barkume, K. M., Ragozzine, D., & Schaller, E. L. 2007, Natur, 446, 294
Brown, M. E., Schaller, E. L., & Fraser, W. C. 2012, AJ, 143, 146
Brown, R. H., Baines, K. H., Bellucci, G., et al. 2004, SSRv, 115, 111
Clark, R. N., Brown, R. H., Jaumann, R., et al. 2005, Natur, 435, 66
Coradini, A., Tosi, F., Gavrishin, A. I., et al. 2008, Icar, 193, 233
Cruikshank, D. P., Meyer, A. W., Brown, R. H., et al. 2010, Icar, 206, 561
Fraser, W. C., & Brown, M. E. 2012, ApJ, 749, 33
Fraser, W. C., Brown, M. E., & Glass, F. 2015, ApJ, 804, 31
Grundy, W. M., Porter, S. B., Benecchi, S. D., et al. 2015, Icar, 257, 130
Guilbert, A., Alvarez-Candal, A., Merlin, F., et al. 2009, Icar, 201, 272
Hansen, G. B., Hollenbeck, E. C., Stephan, K., Apple, S. K., & Shin-White, E.-J. Z. 2012, Icar, 220, 331
Jewitt, D. 2015, AJ, 150, 201
Johnson, T. V., & Lunine, J. I. 2005, Natur, 435, 69
Levison, H. F., Morbidelli, A., Van Laerhoven, C., Gomes, R., & Tsiganis, K. 2008, Icar, 196, 258
Nesvorný, D., Vokrouhlický, D., & Morbidelli, A. 2007, AJ, 133, 1962
Porco, C. C., Baker, E., Barbara, J., et al. 2005, Sci, 307, 1237
Porco, C. C., West, R. A., Squyres, S., et al. 2004, SSRv, 115, 363
Sanchez, J. A., Reddy, V., Nathues, A., et al. 2012, Icar, 220, 36
Simonelli, D. P., Kay, J., Adinolfi, D., et al. 1999, Icar, 138, 249
Tody, D. 1993, in ASP Conf. Ser. 52, Astronomical Data Analysis Software and Systems II, ed. R. J. Hanisch, R. J. V. Brissenden, & J. Barnes (San Francisco, CA: ASP), 173